iScience

CellPress
OPEN ACCESS

Article

Fundamental understanding of nitrogen in biomass electrocatalysts for oxygen reduction and zinc-air batteries

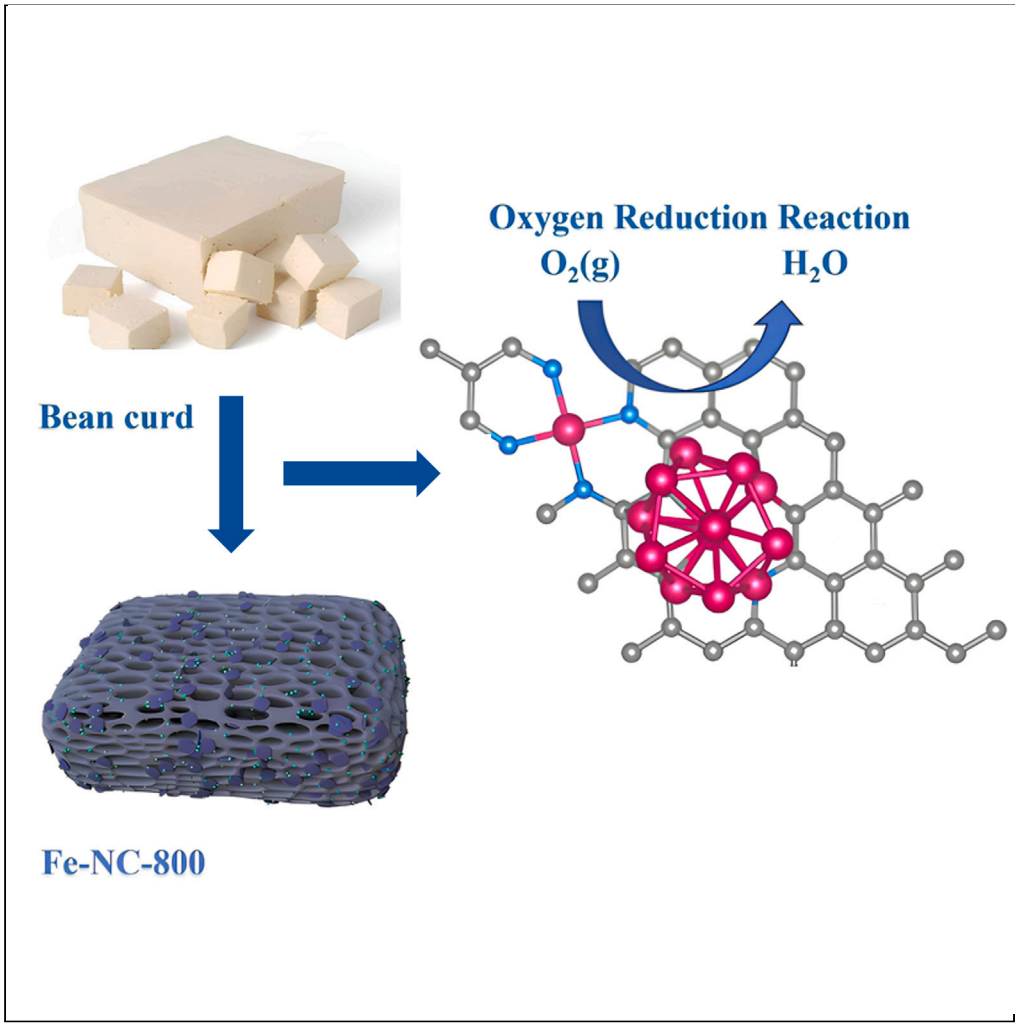

Yue Cao, Yegeng Sun, Haowei Wang, ..., Wentao Lan, Fagang Wang, Ning Han

siweimeng@foxmail.com (W.S.)
lanwentao@sdut.edu.cn (W.L.)
ninghan51@126.com (N.H.)

Highlights

An effective Fe/S/N-doped biomass electrocatalyst was prepared for ORR

This Fe/S/N-doped carbon catalyst was valuable for the Zn-air battery

The different d-band center values are attributed to different N-doped carbon

The active sites on the N-Fe are more natural in terms of the thermodynamics

Cao et al., iScience 27, 108913
February 16, 2024
https://doi.org/10.1016/j.isci.2024.108913

iScience

CellPress
OPEN ACCESS

Article

Fundamental understanding of nitrogen in biomass electrocatalysts for oxygen reduction and zinc-air batteries

Yue Cao,[1,5] Yegeng Sun,[1,5] Haowei Wang,[2] Xue Li,[3] Qing Wang,[1] Weimeng Si,[1,*] Wentao Lan,[1,*] Fagang Wang,[1] and Ning Han[4,6,*]

SUMMARY

Exploring high-efficiency catalysts for oxygen reduction reactions (ORRs) is essential for the development of large-scale applications of fuel cell and metal-air batteries technology. The as-prepared Fe-NC-800 via polymerization-pyrolysis strategy exhibited superior ORR activity with onset potential of 1.030 V vs. reversible hydrogen electrode (RHE) and half-wave potential of 0.908 V vs. RHE, which is higher than that of the Pt/C catalyst and most of other Fe-based catalysts. The different d-band center values can be attributed to the influence of different N-doped carbon, leading to the adjustment in the ORR activity. In addition, Fe-NC-800-based Zn-air battery showed better electrochemical performance with a high discharge specific capacity of 806 mA h g^{-1} and a high-power density of 220 mW cm^{-2} than that of the Pt/C-based battery. Therefore, the biomass Fe-NC-800 catalyst may become a promising substitute for Pt/C catalysts in energy storage and conversion devices.

INTRODUCTION

Storage devices and energy conversion devices, including metal-air batteries (MABs), unitary regenerative fuel cells (URFCs), and fuel cells, are key nodes in the renewable energy development and utilization.[1–5] Oxygen reduction reaction (ORR) on the air cathodes is the key compositions in metal-air batteries as well as reversible fuel cells.[6–9] However, high overpotentials, highly costly and scarce catalysts, and sluggish kinetics limit the large-scale commercialization of fuel cells and MABs.[10–12] Traditionally, Pt-based materials have been known as commercial ORR electrocatalysts.[13,14] Nevertheless, the biggest challenges for Pt-based catalysts are high cost of Pt, CO poisoning effects, and their limited resources.[14–16] Moreover, some Pt-based electrocatalysts have harmful environmental effects caused by undesirable by-products or catalyst residues.[17–19] Therefore, the rational design of Pt-free ORR catalysts for fuel cells with high activity and environmental friendliness in large batches remains a great challenge.

To date, Fe-based ORR catalysts play more and more key role in Pt-free ORR catalysts.[20] Due to superoxo-like O_2 adsorption, Fe-based single site preferentially forms bonding with only one O atom of O_2.[21–24] Theoretical calculation has revealed that Fe clusters could effectively block superoxo-like O_2 adsorption: Fe atoms remain close to each other so that they could form bonding with both O atoms.[22,25] Interestingly, N-doped Fe cluster catalysts exhibit better ORR activity than undoped ORR catalysts.[26–28] Therefore, the coordination environment is crucial for the catalytic performance of iron clusters for ORR reaction. However, Fe clusters coordination environment has been overlooked and few studies have been reported.

Herein, a facile and low-cost strategy of polymerization-pyrolysis strategy (as shown in Figure 1) was reported to enhance the ORR activity of the Fe cluster site in the N, S co-doped non-noble metal catalyst (Fe-NC) using bean curd, $FeCl_3 \cdot 6H_2O$, and pyrrole as precursors. By adjusting the pyrolysis temperature, the content of pyridinic N functional group in the Fe-NC reached the maximum under 800°C. We found that Fe-NC-800 showed superior ORR activity with onset potential (E_{onset}) of 1.030 V vs. RHE and half-wave potential ($E_{1/2}$) of 0.908 V vs. RHE. The reason was that the pyridinic N changed the d-band center of Fe atom. And as a result, the ORR activity was ultimately changed. Moreover, the excellent performance of Fe-NC-800 as air cathode for Zn-air batteries than that of Pt/C catalyst further suggests the viability of Fe-NC-800 in energy storage and conversion devices.

[1]School of Material Science and Engineering, Shandong University of Technology, Zibo 255000, China
[2]Shandong Sunway Chemical Group Co., Ltd, Zibo 255000, China
[3]School of Chemistry and Chemical Engineering, Shandong University of Technology, Zibo 255000, China
[4]Department of Materials Engineering, KU Leuven, Kasteelpark Arenberg 44, 3001 Leuven, Belgium
[5]These authors contributed equally
[6]Lead contact
*Correspondence: siweimeng@foxmail.com (W.S.), lanwentao@sdut.edu.cn (W.L.), ninghan51@126.com (N.H.)
https://doi.org/10.1016/j.isci.2024.108913

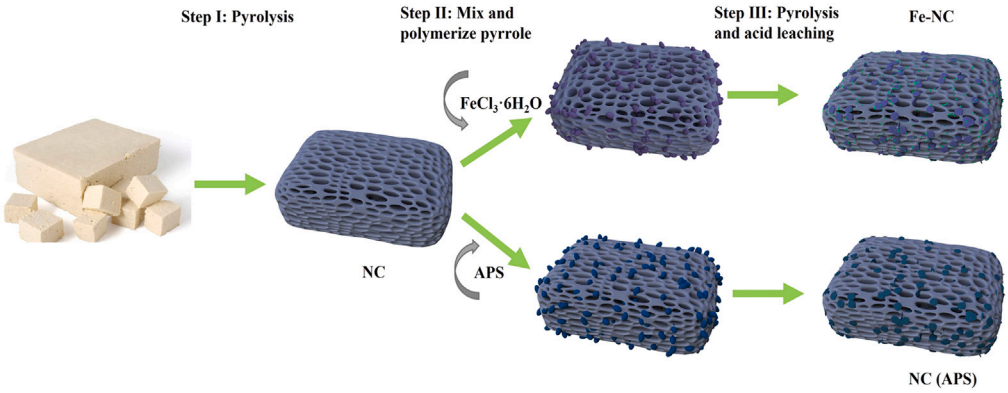

Figure 1. Schematic illustration for the preparation of Fe-NC

RESULTS AND DISCUSSION

Materials preparation and structural characterization

50 g of fresh soybeans were soaked in deionized water overnight at room temperature. The soaked beans were mixed with three times the volume of water in a beaker and then ground in a soymilk machine at high speed for 5 min. The ground slurry was filtered with 120 mesh gauze. The filtered soybean milk is heated to 100°C in a constant-temperature water bath and kept for 15 min. When the boiled soy milk is cooled to room temperature, 0.1 mol/L gluconate-delta-lactone solution was added to 50 mL of soy milk and it was kept at 90°C for 20 min to obtain bean curd. After that, the cooled bean curd was freeze-dried for 24 h. Five grams of bean curd powder was soaked overnight in 10% wt K_2CO_3 solution, followed by filtering and freeze-drying. The product was pyrolyzed in N_2 atmosphere in the range of 700°C–1000°C with a 5°C min^{-1} and kept at the pyrolysis temperatures for 2 h. The resultant product was washed with 0.5 M HCl solution and deionized water and then dried at 80°C. The products were named as NC-X, where X varying from 700 to 1,000 represents the pyrolysis temperatures.

In a typical synthesis, 150 mg of NC-800 and 200 μL of deionized water were mixed and then added into 200 μL of pyrrole, followed by sonicating for 10 min, and stirring vigorously for 10 min. 25 mL of 0.24 M $FeCl_3 \cdot 6H_2O$ solution was added dropwise to the mixed solution by continuous stirring. The mixture is continuously stirred for 4 h to completely polymerize to obtain polypyrrole and washed with deionized water several times. In order to absorb more Fe^{3+}, the resultant product was soaked in the 0.4 M $FeCl_3 \cdot 6H_2O$ solution for 6 h. The Fe^{3+}-saturated product was collected by vacuum filtration and then dried at 80°C for 12 h. The dried product was put into a tube furnace and heated to 800°C with a 5°C min^{-1}. In order to remove the inactive and unstable phases, the prepared products were immersed in 0.5 M HCl solution for 8 h, followed by thoroughly washing with deionized water, filtering, and drying at 80°C overnight. For convenience, the sample is named Fe-NC-800. To optimize experiments about the pyrolysis temperatures, Fe-NC-700, Fe-NC-900, and Fe-NC-1000 were prepared. The synthesis process of NC-800 (APS) was similar to that of Fe-NC-800, with the only difference being that the polymerization initiator was 25 mL of the 0.12 M APS solution (Figure 1).

The morphology of the samples was investigated by scanning electron microscope (SEM) (Figures 2A–2F). After activation, Fe-NC and NC-800 (APS) both exhibited three-dimensional pore structures. However, compared with NC-800 (APS), the rough surface of Fe-NC-800 may be due to the incorporation of iron.[14] In addition, Fe-NC-800 presents a uniform pore structure to further increase the specific surface area, which is conducive to provide more active sites, thereby increasing the oxygen reduction activity.[29,30] Compared with the structure of NC-800 (APS) (Figure S1), Fe-NC-800 sample (Figures 2G and 2H) showed that only a few nanoparticles were dispersed in the final product, which might be related to the acid leaching process.[11,31] The structure of Fe-NC-800 was further analyzed by high-resolution transmission electron microscopy (HRTEM) in Figure 2I. The image displayed obvious lattice fringes. The elemental mapping images of Fe-NC-800 proved the existence of iron in Figure 2M. And it was easy to find that the distributions of C, N, S, and Fe elements in Fe-NC-800 were uniform on the catalyst in Figures 2J–2M.

Chemical state and atomic structure analysis

The porous nature of Fe-NC-800 and the comparative samples were further evaluated by N_2 adsorption-desorption analysis. As shown in Figures 3A and S2, all samples showed an inconspicuous hysteresis loop of type IV, indicating the presence of micropores and mesopores. The specific surface area of the sample reached the maximum at 800°C. With the continuous increase of temperature, the specific surface area decreased, which may be due to the shrinkage of carbon skeleton caused by high temperature.[32] The density functional theory (DFT) pore size distribution also verified that they contained a large number of micropores (Figures 3B and S2). Moreover, the Brunauer-Emmett-Teller (BET) specific surface area and total pore volume of Fe-NC-800 were 1,374 $m^2 g^{-1}$ and 0.74 $m^3 g^{-1}$, respectively, which were larger than those of Fe-NC-700 (700 $m^2 g^{-1}$ and 0.40 $m^3 g^{-1}$), Fe-NC-900 (1,031 $m^2 g^{-1}$ and 0.59 $m^3 g^{-1}$), Fe-NC-1000 (797 $m^2 g^{-1}$ and 0.44 $m^3 g^{-1}$), and NC-800 (APS) (626 $m^2 g^{-1}$ and 0.35 $m^3 g^{-1}$) (Table S1). The high surface area should be mainly attributed to the removal of iron species during the acid leaching process.[14] Since the microporous structure can expose more active sites and the mesoporous structure can promote mass

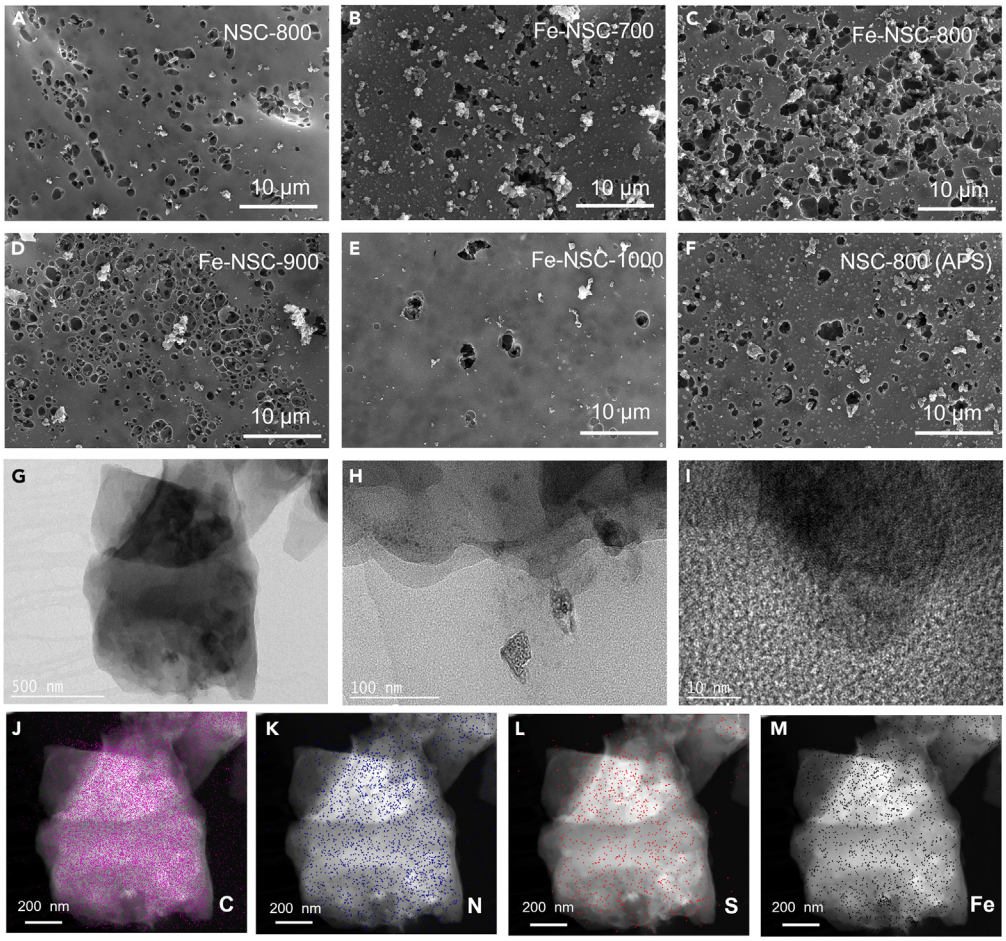

Figure 2. Morphology characteristics of prepared catalysts

(A–F) SEM images of (A) NC-800, (B) Fe-NC-700, (C) Fe-NC-800, (D) Fe-NC-900, (E) Fe-NC-1000, and (F) NC-800(APS).

(G and H) TEM images of Fe-NC-800.

(I) HRTEM image of Fe-NC-800.

(J–M) EDS mapping images of Fe-NC-800 (J) C, (K) N, (L) S, and (M) Fe.

transfer, Fe-NC-800 showed the potential with best ORR catalytic performance among all samples.[10,33,34] The X-ray Diffraction (XRD) patterns of Fe-NC-800 and NC-800 (APS) were shown in Figure 3C, and other samples of different pyrolysis temperature were shown in Figure S2. It can be clearly seen that the two broad peaks were located at 24.9° and 44.0°, corresponding to the (002) and (101) crystal planes of the graphitic carbon, respectively, manifesting that all samples had a partially graphitized amorphous structure.[35–37] Meanwhile, the XRD curves of Fe-NC at different pyrolysis temperatures showed that there were no diffraction peaks related to the crystal planes of the Fe species, suggesting that after the acid leaching process Fe species have been removed.[38] Structural defects of carbon materials are evaluated by Raman spectrum. There are two obvious peaks centered around 1,350 cm^{-1} (D band) and 1,590cm^{-1} (G band).[13,39] The D band represents structural defects of carbon materials, while the G band represents sp^2 hybridization.[40–42] The intensity ratio of D band to G band (I_D/I_G) is used to reflect the degree of structural defects of carbon materials. The higher the I_D/I_G ratio, the higher the degree of defects in the carbon material. As shown in Figures 3D and S2, we found that I_D/I_G increased with increasing pyrolysis temperature which probably can be attributed to the fact that, as pyrolysis temperature increases, the N doping level increases accordingly.[43] However, when the pyrolysis temperature exceeded to 800°C, I_D/I_G tended to decrease due to the increase in graphitization and the removal of some defects for sp^3; the N doping level showed a downward trend. In addition, the I_D/I_G ratio of Fe-NC-800 was 1.04, which was higher than that of NC (APS) (I_D/I_G = 1.00). This Raman results suggested that the introduction of iron into the carbon skeleton induced the formation of defect sites in the carbon matrix. The Raman results showed that Fe-NC-800 had the highest degree of disorder among all the samples, which was of importance for the adsorption of O_2 for ORR.[44]

The elemental compositions of all the samples were further characterized by X-ray photoelectron spectroscopy (XPS) analyses (Figures 3E–3I and S3–S6). As shown in Figure 3E and Table S1, Fe-NC mainly contained C, N, O, S, and Fe elements, suggesting that the Fe element was successfully doped into Fe-NC. As the carbonization temperature increased, the N content decreased and the C content increased. The relative contents of C, N, O, S, and Fe in Fe-NC-800 were approximately 84.15%, 5.14%, 9.78%, 0.43%, and 0.50%, respectively. The

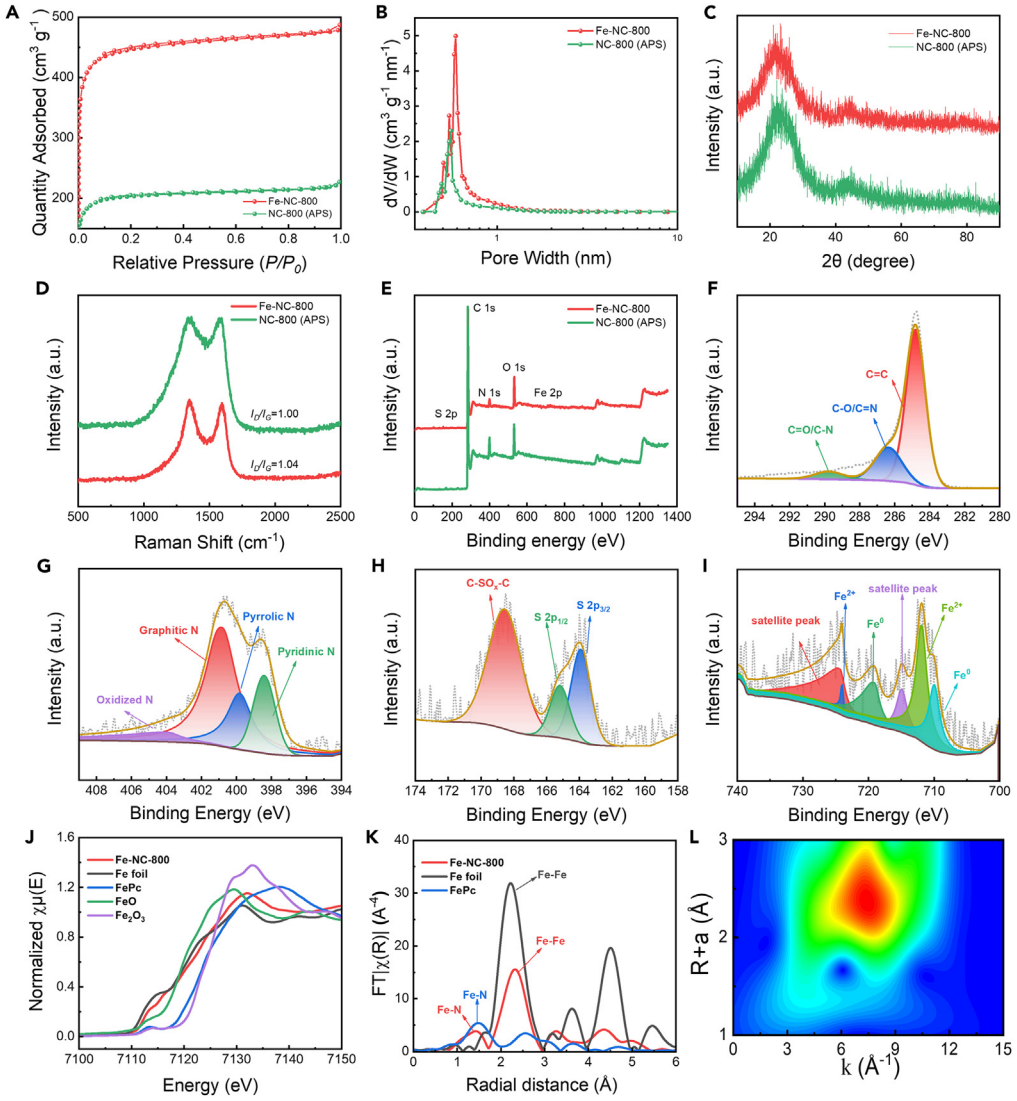

Figure 3. Structural characteristics

(A) N_2 adsorption-desorption curves of Fe-NC-800 and NC-800 (APS).

(B) DFT pore size distributions of Fe-NC-800 and NC-800 (APS).

(C) XRD patterns of Fe-NC-800 and NC-800 (APS).

(D) Raman spectra of Fe-NC-800 and NC-800 (APS).

(E) XPS survey spectra of Fe-NC-800 and NC-800 (APS).

(F–I) High-resolution XPS spectra of Fe-NC-800 (F) C 1s, (G) N1s, (H) S 2p, and (I) Fe 2p.

(J) Fe K-edge XANES spectra of Fe-NC-800, Fe foil, FePc, FeO, and Fe_2O_3.

(K) Fourier transform Fe K-edge EXAFS spectra of Fe-NC-800, Fe foil, and FePc.

(L) Wavelet transform of Fe-NC-800.

high-resolution C 1s spectra of Fe-NC-800 shown in Figure 3F can be deconvoluted into three peaks centered at 284.80, 286.37, and 289.78 eV, illustrating the coexistence of C=C, C-O/C=N, and C=O/C-N, respectively.[45–48] The high-resolution N 1s spectra of Fe-NC-800 (Figure 3G) divided into four peaks correspond to pyridinic N (398.46 eV), pyrrole N (399.53 eV), graphitic N (400.57 eV), and oxidized N (403.26 eV).[49,50] The relative contents of pyridinic N, pyrrole N, graphitic N, and oxidized N were approximately 21.2%, 18.1%, 53.3%, and 7.4%, respectively, shown in Table S2. Pyridinic and pyrrolic N can serve as Fe coordination sites owing to their lone-pair electrons.[30,51,52]

The high-resolution S 2p spectra of Fe-NC-800 (Figure 3H) showed three fitting peaks, which included thiophene-like C-S-C S $2p_{3/2}$ (163.91 eV), C-S-C S $2p_{1/2}$ (165.19 eV), and oxidized S (C-SO_x-C) at 168.55 eV.[53,54] Moreover, the Fe 2p spectra (Figure 3I) could be deconvoluted into six peaks. Fe^0 at 709.97 and 719.12 eV, Fe^{2+} at 711.91 and 724.03 eV, and the peaks at 714.92 and 724.38 eV were satellite peaks.[46,55,56] And the presence of the Fe^0 indicated an existence of Fe clusters in this catalyst.[57] Pyridinic N and pyrrolic N account for 39.3% of the total N atoms. As

the atomic ratio of N is 5.14% (Table S1), our catalyst should contain 2.02% of pyridinic N + pyrrolic N. This leads to the ratio between Fe and N (pyridinic + pyrrolic) to be 0.5:2.02 (approximately 1:4), offering evidence for possible Fe-N_4 structure formation.[58]

To further understand the local atomic coordination and electronic structure of metallic Fe in Fe-NC-800, extended X-ray absorption fine structure (EXAFS) was recorded. Figure 3J is the XANES spectrum of Fe-NC-800 and reference samples, such as Fe foil, Fe_2O_3, FeO, and iron phthalocyanie (FePc). The near-edge absorption threshold of Fe K-edge of Fe-NC-800 was between that of Fe foil and FeO, implying that Fe possesses an oxidation state between 0 and +2. What is more, the white-line intensity of atomic clusters decorated Fe-NC-800 was higher than that of Fe foil, which meant electronic structure of Fe cluster was modulated by the introduced N-doped carbon.[59] The Fourier transform (FT) EXAFS spectra of Fe-NC-800 (Figure 3K) presented a primary peak located at ~1.5 Å, corresponding to the Fe−N(O) scattering path, and there was a strong peak around 2.1 Å, corresponding to the Fe-Fe bond.[60,61] This result indicated that Fe-N(O) coexists with Fe clusters. The Fe-N electronic structure can be modulated by the introduced clusters, which is beneficial to the oxygen adsorption and product desorption in Fe-NC-800, thereby enhancing the catalytic activity.[62,63] Moreover, the shell Fe-Fe bond at 4.4 Å was weak indicating that had reduced structural periodicity and the size of the Fe clusters was very small.[64] Since the peak positions of Fe-N and Fe-O are very close in EXAFS,[59] in order to better understand the resolution of K space, we fitted wavelet transform (WT) EXAFS analyses of Fe-NC-800 catalysts to analyze backscattered atoms, shown in Figure 3L. The WT maxima of Fe–Fe and Fe–N coordination in Fe-NC-800 were located at 3.8 $Å^{-1}$ and 7.0 $Å^{-1}$, respectively.[61,65] Stretched WT maxima at 3.8–7.0 $Å^{-1}$ observed in Fe-NC-800 clearly confirmed the coexistence of Fe–N and Fe–Fe bonds. It is worth noting that the contribution of Fe-Fe path scattering in Fe-NC-800 was stronger than that of Fe-N. The Fe-Fe coordination was the active center in Fe-NC-800, and the Fe-N bond acts as a bridge connecting the Fe clusters and the carbon matrix. Although the strength of the Fe-N region in WT-EXAFS was weak, compared with Fe foil, there was still an obvious bonding region.

Electrocatalytic ORR performances

To evaluate the electrocatalytic activity of the prepared catalysts, cyclic voltammetry (CV) test and linear sweep voltammetry (LSV) test were performed on a rotating disk electrode (RDE) in alkaline solution. Two important parameters of LSV, onset potential (E_{onset}) and half-wave potential ($E_{1/2}$), were used to assess the ORR activity in O_2-saturated 0.1 M KOH solution.[15,66] Previous studies have shown that pyrolysis temperature is greatly important for the performance of carbon-based electrocatalysts.[32,67] Therefore, the oxygen reduction performance of the Fe-NC catalyst as a function of the pyrolysis temperature in the 700°C–1,000°C range was first screened by RDE in O_2-saturated 0.1 M KOH solution. All the four catalysts exhibited ORR catalytic activity with obvious cathodic peak in O_2-saturated 0.1 M KOH solution vs. a N_2-saturated electrolyte and compared with other samples (Figure 4A). The reduction peak potential displayed a decrease in the order of Fe-NC-800 > Fe-NC-900 > Fe-NC-1000 > Fe-NC-700, confirming that the oxygen reduction activity reached the highest under 800°C.

Furthermore, the ORR performances of NC-800 (APS), Fe-NC-800, and Pt/C were tested to further understand the roles of Fe and N in the carbon skeleton during the oxygen reduction process. As shown in Figure 4A, it was also distinct that the three catalysts in the CV loops had developed cathode peaks. The peak potential at 0.890 V vs. RHE provided by the Fe-NC-800 catalyst was much higher than that of the NC-800 (APS) (0.731 V vs. RHE) and even comparable to that of the Pt/C (0.901 V vs. RHE) in O_2-saturated 0.1 M KOH solution, indicating that Fe-NC-800 exhibited excellent ORR activity. LSV curves of the three samples were shown in Figure 4B. NC-800(APS) exhibited the worst ORR activity with the lowest onset potential of 0.874 V vs. RHE and half-wave potential of 0.739 V vs. RHE (Figure 4C; Table S3), which may be due to its low specific surface area and underdeveloped pore structure. And the low specific surface area can expose fewer active sites.[51] Fe-NC-800 showed an onset potential of 1.030 V vs. RHE and a half-wave potential of 0.908 V vs. RHE (Figure 4C). The LSV curves were used to further evaluate the oxygen reduction activity of the Fe-NC-700, Fe-NC-800, Fe-NC-900, and Fe-NC-1000 catalysts. Fe-NC-800 shows the best onset potential and half-wave potential ORR performance among all Fe-NC catalysts (Figures 4B and 4C). Because the specific surface area (1,374 $m^2\ g^{-1}$) and disorder degree (I_D/I_G = 1.04) of the sample reached the maximum under 800°C, more defect active sites can be produced.[68] Moreover, the Fe-NC-800 catalyst exhibited snug pores, which were suitable for the transportation of electrolytes.[46] Therefore, this study suggested that the superior ORR catalytic activity of Fe-NC-800 can be attributed to optimization of multiple factors.

The kinetics of ORR was investigated by RDE to further understand the reaction pathway of ORR from 625 rpm to 2,025 rpm. The LSV curves of Fe-NC-800, NC-800 (APS), and Pt/C at different rotation rates were shown in Figure S7. As the diffusion distance became short at high speeds, the current density of Fe-NC-800 increased with the increase in rotation speeds,[69] shown in Figure S7. The corresponding Koutecky–Levich (K-L) plots obtained by fitting the LSV curve exhibited fine linearity between 0.2 and 0.6 V vs. RHE, suggesting the first-order reaction kinetics toward the dissolved oxygen concentration.[70,71] Between 0.2 and 0.6 V vs. RHE, the electron transfer number of Fe-NC-800 was 3.99, indicating that the ORR process was dominated by direct four-electron pathway, similar to the catalytic pathways of Pt/C catalysts (n ≈ 4.00).[6] In comparison, the electron transfer number of NC-800 (APS) was 2.81 (Figure S8), which means that the NC-800 (APS) electrode underwent a "two-step peroxide" reduction process.[72] On the other hand, the Tafel slope (Figure 4D) of Fe-NC-800 was 74 mV dec^{-1}, much lower than that of NC-800(APS) (109 mV dec^{-1}), which was comparable to that of Pt/C (65 mV dec^{-1}), manifesting that the Fe-NC-800 exhibited excellent ORR kinetics similar to Pt/C catalyst. In addition, as shown in Figure S9, at the potential range of 0.2–0.6 V, electron transfer number (n) of Fe-NC-800 was calculated to be 3.99, much higher than that of the other prepared catalysts (n ≈ 3.44 for Fe-NC-700, n ≈ 3.95 for Fe-NC-900, and n ≈ 3.57 for Fe-NC-1000), suggesting a complete four-electron transfer process. As shown in Figure 4E, Fe-NC-800 had superior oxygen reduction kinetics even comparable to that of Pt/C. Accordingly, the Fe-NC-800 catalyst was used for discussion in the following.

The durability of ORR catalysts is an important concern for potential fuel cell. The durability of Fe-NC-800 and Pt/C was tested at a rotation rate of 1,600 rpm for 20,000 s by the chronoamperometric measurements, as shown in Figure 4F. The Fe-NC-800 catalyst maintained 89% of the initial current density after continuous measurements for 20,000 s, much larger than that of Pt/C of 78%, suggesting that the Fe-NC-800

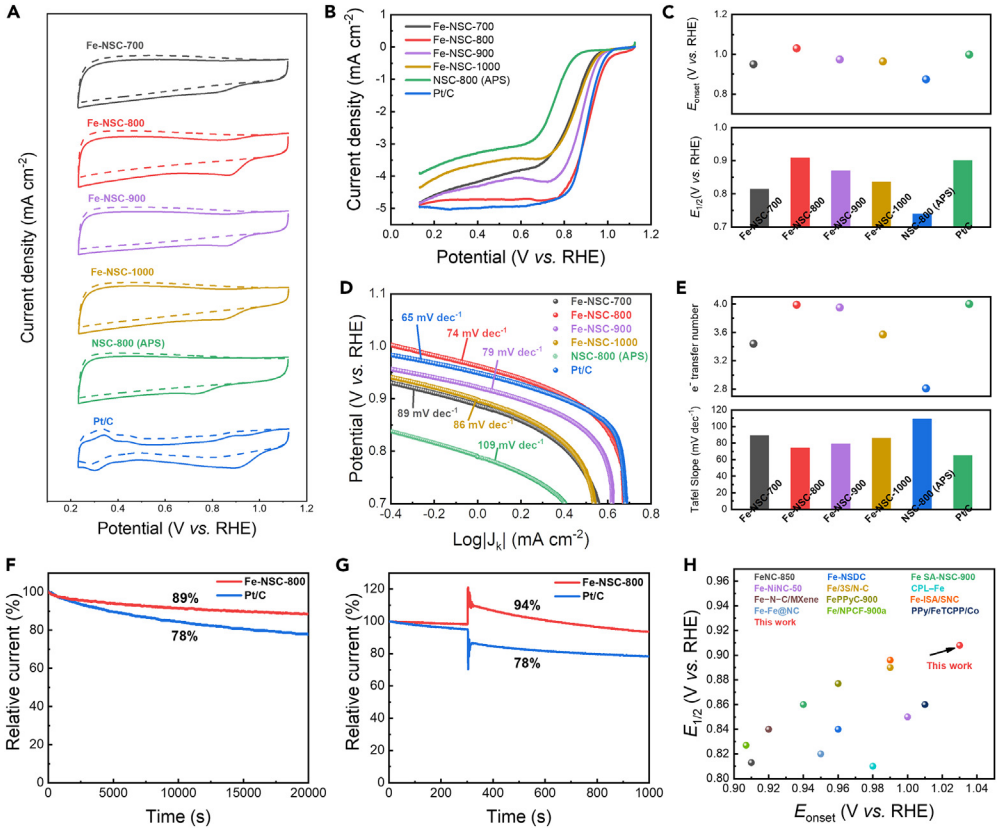

Figure 4. Electrochemical ORR test

(A and B) CV (A) and LSV (B) of prepared catalysts.

(C) ORR performance parameters including onset potential and half-wave potential of Fe-NC-700, Fe-NC-800, Fe-NC-900, Fe-NC-1000, NC-800 (APS), and Pt/C catalysts.

(D) Comparison of ORR performances for Fe-NC-800 and other reported Fe-based ORR catalysts.

(E and F) ORR Tafel slopes (E) obtained from the LSV curves and (F) ORR kinetics parameters including electron transfer number and Tafel slope of Fe-NC-700, Fe-NC-800, Fe-NC-900, Fe-NC-1000, NC-800 (APS), and Pt/C catalysts.

(G and H) Chronoamperometric curves (G) and methanol tolerance (H) of the Fe-NC-800 catalyst and Pt/C in O_2-saturated 0.1 M KOH solution.

catalyst had better long-term durability than Pt/C catalyst in the 0.1 M KOH solution. It is well known that the methanol-tolerant ability is of importance. Therefore, the ethanol-tolerant measurements on the Fe-NC-800 electrode were carried out. After injecting methanol and continuing the test for 700 s, the loss of initial current density Fe-NC-800 catalyst was 6% (Figure 4G), smaller than that of Pt/C electrode, which suggested that the Fe-NC-800 catalyst had excellent catalytic selectivity. The ORR parameters of Fe-NC-800 were higher than those of the Pt/C catalyst (E_{onset} = 0.999 V vs. RHE and $E_{1/2}$ = 0.876 V vs. RHE) and most of other Fe-based ORR catalysts[15,30,32,61,68,73–79] (Figure 4H), which further manifested its superior ORR activity. The superior ORR catalytic activity of Fe-NC-800 may be firstly due to its developed porous structure and abundant catalytically active sites such as Fe-N_x, to facilitate efficient mass transfer.[80] Secondly, bean curd-derived carbon material itself contains a large amount of sulfur. The large number of defect sites produced by the doping of sulfur into the carbon support can coordinate the electronic properties and surface properties of Fe-NC-800, thereby optimizing the electrochemical catalytic reactions and increasing reactions reactivity.[68]

Insights into electrocatalysis mechanism

DFT calculations were performed to gain an atomic insight into the ORR performance of Fe-NC. Three ideal models representing graphitic N, pyridinic N, and pyrrole N, defined as gN-Fe, prN-Fe, and pdN-Fe, respectively, were constructed by the corresponding N-doped carbon and Fe cluster proposed in calculation (Figure S10). The ORR catalytic activity of the materials was studied by calculating the adsorption properties of the materials to the reaction intermediates (Figures S11–S13). As shown in the free energy diagram (Figure 5A), by calculating the free energy difference at potential of 1.23 V, the last step is identified to possess the highest free energy difference, indicating that the step from adsorbed OH* to H_2O at active sites is the rate-determine step (RDS).[77] The free energy change of pdN-Fe (1.43 eV) is lower than that of prN-Fe (1.72 eV) and gN-Fe (1.83 eV), suggesting the active sites on the pdN-Fe is more natural in terms of the thermodynamics.[59,73]

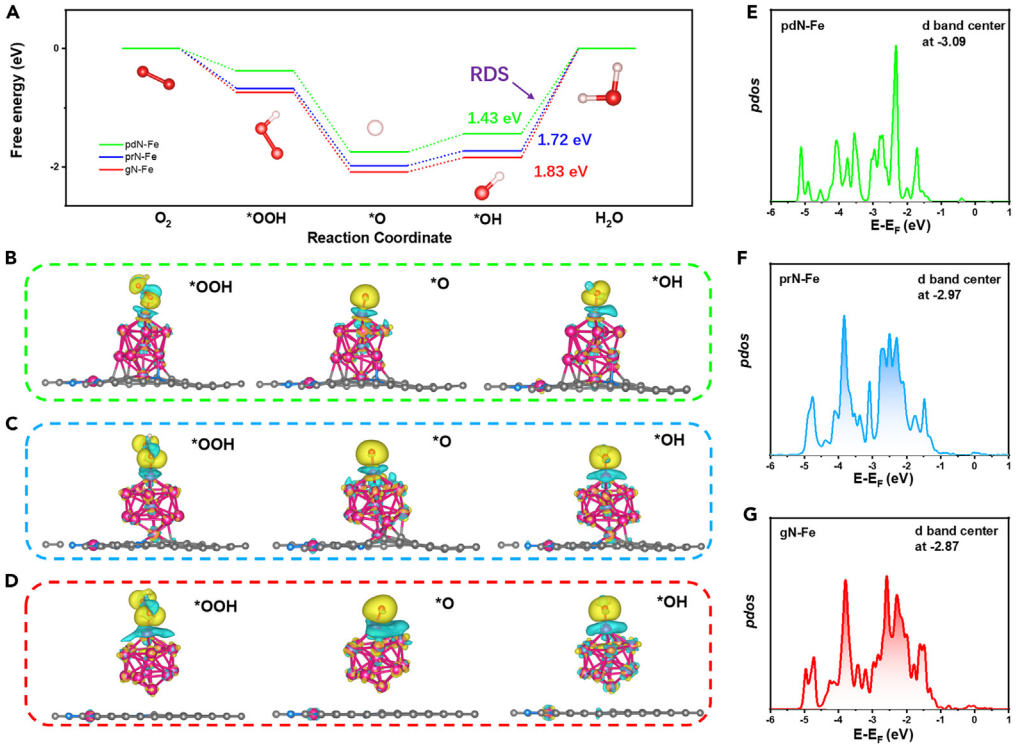

Figure 5. Theoretical analysis

(A) Free energy diagram of ORR for pdN-Fe, prN-Fe, and gN-Fe at 1.23 V vs. CHE.

(B–D) Side views of differential charge density of (B) pdN-Fe, (C) prN-Fe, and (D) gN-Fe (yellow and cyan represent the accumulation and depletion of charge density, respectively).

(E–G) PDOS of Fe d orbitals in (E) pdN-Fe, (F) prN-Fe, and (G) gN-Fe.

According to the free energy diagram of ORR at potential of 1.23 V, the uphill free energy of the RDS suggesting the weaker bonding of -OH has potential to improve the ORR activity. To further reveal the electron redistribution behavior, charge density difference analyses are calculated and shown in Figures 5B–5D and S13. In various structures, the charge transfer between the adsorbates with the structure can be observed. The most charge transfer can be found on gN-Fe, suggesting the strongest bonding between the adsorbates and gN-Fe (Figures 5D and S14). On the other hand, the minimum charge transfer on pdN-Fe means that the bond between the adsorbent and PdN-Fe is weakest[73] (Figures 5B and S13). This result is also consistent with the analysis of free energy. The analysis of charge density difference indicates that the Fe cluster with the pdN can effectively promote the ORR activity.

The d-band center of Fe atom and its electron occupation can influence the binding strength between adsorbates and active sites. The total density of states (TDOS) and the projected density of states (PDOS) of Fe 3d orbitals of pdN-Fe, prN-Fe, and gN-Fe were calculated and displayed in Figures S15 and 5E–5G. The different d-band center values can be attributed to the influence of difference N-doped carbon, as mentioned before. The d-band center of Fe in pdN-Fe (−3.09 eV) is negatively compared to that in prN-Fe (−2.97 eV) and gN-Fe (−2.87 eV), indicating that the interaction strength between adsorbates and active sites decreases in pdN-Fe, endowing it with an optimized bonding property and facilitating the desorption of *OH from active sites for ORR.

Zn-air batteries performance

Encouraged by the excellent electrocatalytic activity toward ORR of Fe-NC-800 catalyst, we further constructed Zn-air battery using Fe-NC-800 catalyst-loaded nickel foam as air cathode to demonstrate its viability in actual battery devices. Figure 6A showed a schematic diagram of the structure of Zn-air battery. As shown in Figure S16, the open circuit potential of the Fe-NC-800-based Zn-air battery was about 1.531 V, which was higher than that of Pt/C-based Zn-air battery (1.460 V). The charge-discharge voltage gap of Fe-NC-800-based Zn-air battery was lower than that of Pt/C-based Zn-air battery (Figure 6B), which proved its remarkable rechargeability.[30] In Figure 6C, the Fe-NC-800-based Zn-air battery showed a peak power density of 220 mW cm^{-2}, which was 1.31 times that of Pt/C-based battery (168 mW cm^{-2}) and higher than the power density of other reported Fe-based catalysts (Table S4). In order to evaluate the capacity of the battery, galvanostatic discharge curves of the Fe-NC-800-based and Pt/C-based Zn-air battery at a current density of 10 mA cm^{-2} are shown in Figure 6D. The Fe-NC-800-based Zn-air battery generated a discharge specific capacity of 806 mA h g^{-1}, which was larger than that of Pt/C-based Zn-air battery (723 mA h g^{-1}).

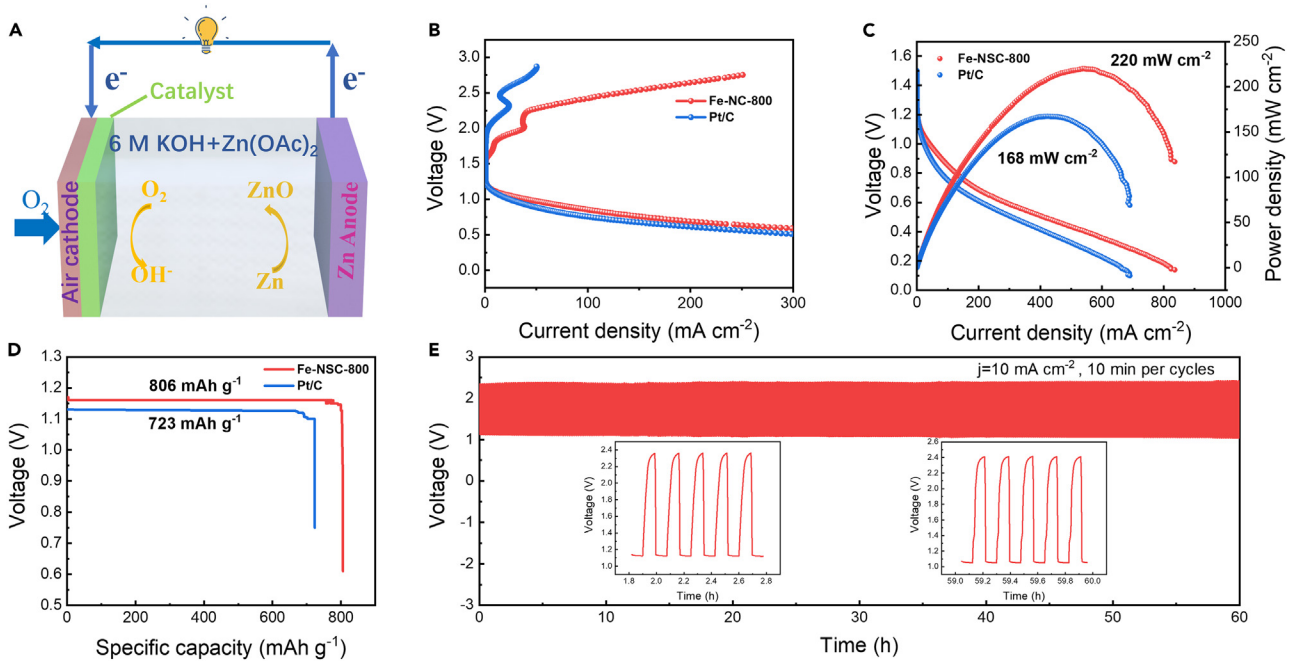

Figure 6. Zn-air battery

(A) Schematic diagram of a Zn-air battery.

(B) Charge and discharge polarization curves of Fe-NC-800 and Pt/C.

(C) polarization curves and corresponding power density plots of Zn-air battery using Fe-NC-800 and Pt/C catalysts as air electrode.

(D) The galvanostatic discharge curves of the Fe-NC-800-based and Pt/C-based Zn-air battery at a current density of 10 mA cm^{-2}.

(E) Galvanostatic charge-discharge cycling curves using Fe-NC-800 catalysts as air electrode at 10 mA cm^{-2} with 10 min cycle.

Moreover, the cycling performance of the Fe-NC-800-based Zn-air battery has been estimated from galvanostatic charge/discharge curves at 10 mA cm^{-2}. To compare with Pt/C, the measured voltage gap of Fe-NC-800 had not obvious loss during the cycling process, indicating that Fe-NC-800 had good cycling performance for Zn-air batteries (Figure 6E). Moreover, compared with Pt/C, Fe-NC-800 demonstrates good cycling stability (Figure S17).

Conclusions

In summary, a new and effective "polymerization-pyrolysis" strategy was developed to fabricate Fe/S co-doped non-noble metal catalyst (Fe-NC) using bean curd as nitrogen and sulfur source. Such a novel strategy not only can provide a large specific surface area of Fe-NC but also improved the degree of defects of Fe-NC, which was beneficial to the ORR. The electrochemical measurements showed that the prepared Fe-NC-800 catalyst exhibited excellent electrocatalytic ORR activity in alkaline media, even comparable to that of the commercial Pt/C catalyst, and superior stability and methanol tolerance. Fe-NC-800-based Zn-air battery possessed better performance than the Pt/C-based one with higher peak power density and larger specific capacity. The novel strategy of bean curd-derived Fe-NC-800 catalyst may inspire new thoughts and design to prepare non-precious electrocatalysts applied in fuel cell.

STAR★METHODS

Detailed methods are provided in the online version of this paper and include the following:

- KEY RESOURCES TABLE
- RESOURCE AVAILABILITY
  - Lead contact
  - Materials availability
  - Data and code availability
- METHOD DETAILS
  - Material synthesis and characterization

SUPPLEMENTAL INFORMATION

Supplemental information can be found online at https://doi.org/10.1016/j.isci.2024.108913.

ACKNOWLEDGMENTS

This work was supported by the National Natural Science Foundation of China (51502161, 51572127, and 21576138), the Natural Science Foundation of Shandong Province (ZR2014EMQ008, ZR2021QE152, 2023TSGC0484), Natural Science Foundation of Jiangsu Province (BK20160828), Jiangsu Postdoctoral Science Foundation (1501016B), and the Science & Technology Plan of the Education Department of Shandong Province (J15LA08, J16LA07, and J11LD12). The authors would like to thank Conghua Qi from Shiyanjia Lab (www.shiyanjia.com) for the XPS and EXAFS analysis.

AUTHOR CONTRIBUTIONS

Y.C. and N.H. proposed the research idea, conceived the study, designed the experiments, coordinated the work, and performed the mechanism analysis. Y.C. and Y.S. conducted electrochemistry measurement. H.W., X.L., and W.L. conducted TEM and XANES. Q.W. helped with the visualization of the experiment results. W.S. and Y.C. assisted in the first-principles calculation. Y.C. and Y.S. wrote the manuscript; F.W. and N.H. revised the manuscript. W.S., W.L., and N.H. supervised the work and supported with the resource. All co-authors contributed to this work.

DECLARATION OF INTERESTS

The authors declare no competing interests.

Received: June 27, 2023
Revised: December 14, 2023
Accepted: January 10, 2024
Published: January 15, 2024

REFERENCES

1. Li, Z., He, H., Cao, H., Sun, S., Diao, W., Gao, D., Lu, P., Zhang, S., Guo, Z., Li, M., et al. (2019). Atomic Co/Ni dual sites and Co/Ni alloy nanoparticles in N-doped porous Janus-like carbon frameworks for bifunctional oxygen electrocatalysis. Appl. Catal. B Environ. *240*, 112–121.
2. Wang, H.-F., and Xu, Q. (2019). Materials Design for Rechargeable Metal-Air Batteries. Matter *1*, 565–595.
3. Wang, Y.-J., Fang, B., Wang, X., Ignaszak, A., Liu, Y., Li, A., Zhang, L., and Zhang, J. (2018). Recent advancements in the development of bifunctional electrocatalysts for oxygen electrodes in unitized regenerative fuel cells (URFCs). Prog. Mater. Sci. *98*, 108–167.
4. Han, N., Feng, S., Liang, Y., Wang, J., Zhang, W., Guo, X., Ma, Q., Liu, Q., Guo, W., Zhou, Z., et al. (2023). Achieving efficient electrocatalytic oxygen evolution in acidic media on yttrium ruthenate pyrochlore through cobalt incorporation. Adv. Funct. Mater. *33*, 2208399.
5. Wang, Q., Han, N., Bokhari, A., Li, X., Cao, Y., Asif, S., Shen, Z., Si, W., Wang, F., Klemeš, J.J., and Zhao, X. (2022). Insights into MXenes-based electrocatalysts for oxygen reduction. Energy *255*, 124465.
6. Han, N., Zhang, W., Guo, W., Pan, H., Jiang, B., Xing, L., Tian, H., Wang, G., Zhang, X., and Fransaer, J. (2023). Designing Oxide Catalysts for Oxygen Electrocatalysis: Insights from Mechanism to Application. Nano-Micro Lett. *15*, 185.
7. Cao, Y., Sun, Y., Han, N., Li, X., Wang, Q., Sun, K., Si, W., Wang, F., Zhao, X., Bokhari, A., et al. (2023). Novel highly active and selective CoNSC efficient ORR catalyst derived from in-situ egg gel pyrolysis. Fuel *333*, 126432.
8. Zhang, J., Chen, Y., Liu, Y., Liu, X., and Gao, S. (2022). Self-catalyzed growth of Zn/Co-N-C carbon nanotubes derived from metal-organic frameworks as efficient oxygen reduction catalysts for Zn-air battery. Sci. China Mater. *65*, 653–662.
9. Jiao, C., Xu, Z., Shao, J., Xia, Y., Tseng, J., Ren, G., Zhang, N., Liu, P., Liu, C., Li, G., et al. (2023). High-Density Atomic Fe–N4/C in Tubular, Biomass-Derived, Nitrogen-Rich Porous Carbon as Air-Electrodes for Flexible Zn–Air Batteries. Adv. Funct. Mater. *33*, 2213897.
10. Zhang, Z., Gao, X., Dou, M., Ji, J., and Wang, F. (2017). Biomass Derived N-Doped Porous Carbon Supported Single Fe Atoms as Superior Electrocatalysts for Oxygen Reduction. Small *13*, 1604290.
11. Nallathambi, V., Lee, J.-W., Kumaraguru, S.P., Wu, G., and Popov, B.N. (2008). Development of high performance carbon composite catalyst for oxygen reduction reaction in PEM Proton Exchange Membrane fuel cells. J. Power Sources *183*, 34–42.
12. Tian, X., Lu, X.F., Xia, B.Y., and Lou, X.W.D. (2020). Advanced Electrocatalysts for the Oxygen Reduction Reaction in Energy Conversion Technologies. Joule *4*, 45–68.
13. Li, B., Geng, D., Lee, X.S., Ge, X., Chai, J., Wang, Z., Zhang, J., Liu, Z., Hor, T.S.A., and Zong, Y. (2015). Eggplant-derived microporous carbon sheets: towards mass production of efficient bifunctional oxygen electrocatalysts at low cost for rechargeable Zn-air batteries. Chem. Commun. *51*, 8841–8844.
14. Zhang, J., Wu, S., Chen, X., Pan, M., and Mu, S. (2014). Egg derived nitrogen-self-doped carbon/carbon nanotube hybrids as noble-metal-free catalysts for oxygen reduction. J. Power Sources *271*, 522–529.
15. Peng, X., Taie, Z., Liu, J., Zhang, Y., Peng, X., Regmi, Y.N., Fornaciari, J.C., Capuano, C., Binny, D., Kariuki, N.N., et al. (2020). Hierarchical electrode design of highly efficient and stable unitized regenerative fuel cells (URFCs) for long-term energy storage. Energy Environ. Sci. *13*, 4872–4881.
16. Cheng, H., Wu, X., Feng, M., Li, X., Lei, G., Fan, Z., Pan, D., Cui, F., and He, G. (2021). Atomically Dispersed Ni/Cu Dual Sites for Boosting the CO2 Reduction Reaction. ACS Catal. *11*, 12673–12681.
17. Cao, Y., Sun, Y., Zheng, R., Wang, Q., Li, X., Wei, H., Wang, L., Li, Z., Wang, F., and Han, N. (2023). Biomass-derived carbon material as efficient electrocatalysts for the oxygen reduction reaction. Biomass Bioenergy *168*, 106676.
18. Zhang, J., Wu, S., Chen, X., Cheng, K., Pan, M., and Mu, S. (2014). An animal liver derived non-precious metal catalyst for oxygen reduction with high activity and stability. RSC Adv. *4*, 32811.
19. Zhao, Y., Liu, Y., Chen, Y., Liu, X., Li, X., and Gao, S. (2021). A treasure map for nonmetallic catalysts: optimal nitrogen and fluorine distribution of biomass-derived carbon materials for high-performance oxygen reduction catalysts. J. Mater. Chem. A Mater. *9*, 18251–18259.
20. Martinez, U., Komini Babu, S., Holby, E.F., Chung, H.T., Yin, X., and Zelenay, P. (2019). Progress in the development of Fe-based PGM-free electrocatalysts for the oxygen reduction reaction. Adv. Mater. *31*, 1806545.
21. Ye, W., Chen, S., Lin, Y., Yang, L., Chen, S., Zheng, X., Qi, Z., Wang, C., Long, R., Chen, M., et al. (2019). Precisely tuning the number of Fe atoms in clusters on N-doped carbon toward acidic oxygen reduction reaction. Chem *5*, 2865–2878.
22. Chen, Y., Ji, S., Wang, Y., Dong, J., Chen, W., Li, Z., Shen, R., Zheng, L., Zhuang, Z., Wang, D., and Li, Y. (2017). Isolated single iron atoms anchored on N-doped porous carbon as an efficient electrocatalyst for the oxygen reduction reaction. Angew. Chem., Int. Ed. Engl. *56*, 6937–6941.
23. Yang, T., Chen, Y., Liu, Y., Liu, X., and Gao, S. (2022). Self-sacrificial template synthesis of Fe, N co-doped porous carbon as efficient

oxygen reduction electrocatalysts towards Zn-air battery application. Chin. Chem. Lett. *33*, 2171–2177.
24. Li, Z., Tian, Z., Cheng, H., Wang, T., Zhang, W., Lu, Y., Lai, Y., and He, G. (2023). Engineering d-band center of FeN4 moieties for efficient oxygen reduction reaction electrocatalysts. Energy Storage Mater. *59*, 102764.
25. Wan, X., Liu, Q., Liu, J., Liu, S., Liu, X., Zheng, L., Shang, J., Yu, R., and Shui, J. (2022). Iron atom–cluster interactions increase activity and improve durability in Fe–N–C fuel cells. Nat. Commun. *13*, 2963.
26. Liu, M., Lee, J., Yang, T.C., Zheng, F., Zhao, J., Yang, C.M., and Lee, L.Y.S. (2021). Synergies of Fe single atoms and clusters on N-doped carbon electrocatalyst for pH-universal oxygen reduction. Small Methods *5*, 2001165.
27. Xue, H., He, T., Chabu, J.M., Liu, J., Wu, H., Zheng, J., Tan, M., Ma, J., Shen, R., Deng, L., and Zhang, Y. (2018). Iron Single Clusters Anchored on N-Doped Porous Carbon as Superior Trace-Metal Catalysts toward Oxygen Reduction. Adv. Mater. Interfac. *5*, 1701345.
28. Liu, D., He, Y., Qiu, W., Peng, X., Li, M., Li, D., Pu, J., Yang, J., Gan, Y., Yang, G., et al. (2023). Management of Host–Guest Triplet Exciton Distribution for Stable, High-Efficiency, Low Roll-Off Solution-Processed Blue Organic Light-Emitting Diodes by Employing Triplet-Energy-Mediated Hosts. Adv. Funct. Mater. *33*, 2301327.
29. Zhang, J., Zhang, C., Zhao, Y., Amiinu, I.S., Zhou, H., Liu, X., Tang, Y., and Mu, S. (2017). Three dimensional few-layer porous carbon nanosheets towards oxygen reduction. Appl. Catal. B Environ. *211*, 148–156.
30. Zhang, J., Zhang, M., Zeng, Y., Chen, J., Qiu, L., Zhou, H., Sun, C., Yu, Y., Zhu, C., and Zhu, Z. (2019). Single Fe Atom on Hierarchically Porous S, N-Codoped Nanocarbon Derived from Porphyra Enable Boosted Oxygen Catalysis for Rechargeable Zn-Air Batteries. Small *15*, e1900307.
31. Guo, C.-Z., Liao, W.-L., and Chen, C.-G. (2014). Design of a non-precious metal electrocatalyst for alkaline electrolyte oxygen reduction by using soybean biomass as the nitrogen source of electrocatalytically active center structures. J. Power Sources *269*, 841–847.
32. Yang, J., Hu, J., Weng, M., Tan, R., Tian, L., Yang, J., Amine, J., Zheng, J., Chen, H., and Pan, F. (2017). Fe-Cluster Pushing Electrons to N-Doped Graphitic Layers with Fe3C(Fe) Hybrid Nanostructure to Enhance O2 Reduction Catalysis of Zn-Air Batteries. ACS Appl. Mater. Interfaces *9*, 4587–4596.
33. Liang, H.W., Zhuang, X., Brüller, S., Feng, X., and Müllen, K. (2014). Hierarchically porous carbons with optimized nitrogen doping as highly active electrocatalysts for oxygen reduction. Nat. Commun. *5*, 4973.
34. Pampel, J., and Fellinger, T.-P. (2016). Opening of Bottleneck Pores for the Improvement of Nitrogen Doped Carbon Electrocatalysts. Adv. Energy Mater. *6*.
35. Zhang, W., Sherrell, P., Minett, A.I., Razal, J.M., and Chen, J. (2010). Carbon nanotube architectures as catalyst supports for proton exchange membrane fuel cells. Energy Environ. Sci. *3*, 1286.
36. Guo, C., Liao, W., Li, Z., and Chen, C. (2015). Exploration of the catalytically active site structures of animal biomass-modified on cheap carbon nanospheres for oxygen reduction reaction with high activity, stability and methanol-tolerant performance in alkaline medium. Carbon *85*, 279–288.
37. Hao, Y., Zhang, X., Yang, Q., Chen, K., Guo, J., Zhou, D., Feng, L., and Slanina, Z. (2018). Highly porous defective carbons derived from seaweed biomass as efficient electrocatalysts for oxygen reduction in both alkaline and acidic media. Carbon *137*, 93–103.
38. Li, M., Xiong, Y., Liu, X., Han, C., Zhang, Y., Bo, X., and Guo, L. (2015). Iron and nitrogen co-doped carbon nanotube@hollow carbon fibers derived from plant biomass as efficient catalysts for the oxygen reduction reaction. J. Mater. Chem. A Mater. *3*, 9658–9667.
39. Pei, Z., Li, H., Huang, Y., Xue, Q., Huang, Y., Zhu, M., Wang, Z., and Zhi, C. (2017). Texturing in situ: N,S-enriched hierarchically porous carbon as a highly active reversible oxygen electrocatalyst. Energy Environ. Sci. *10*, 742–749.
40. Guo, Z., Kong, X., Wu, X., Xing, W., Zhou, J., Zhao, Y., and Zhuo, S. (2020). Heteroatom-doped hierarchical porous carbon via molten-salt method for supercapacitors. Electrochim. Acta *360*, 137022.
41. Hou, J., Jiang, K., Tahir, M., Wu, X., Idrees, F., Shen, M., and Cao, C. (2017). Tunable porous structure of carbon nanosheets derived from puffed rice for high energy density supercapacitors. J. Power Sources *371*, 148–155.
42. Pan, F., Cao, Z., Zhao, Q., Liang, H., and Zhang, J. (2014). Nitrogen-doped porous carbon nanosheets made from biomass as highly active electrocatalyst for oxygen reduction reaction. J. Power Sources *272*, 8–15.
43. Zhang, M., Song, Y., Tao, H., Yan, C., Masa, J., Liu, Y., Shi, X., Liu, S., Zhang, X., and Sun, Z. (2018). Lignosulfonate biomass derived N and S co-doped porous carbon for efficient oxygen reduction reaction. Sustain. Energy Fuels *2*, 1820–1827.
44. Zhou, X., Bai, Z., Wu, M., Qiao, J., and Chen, Z. (2015). 3-Dimensional porous N-doped graphene foam as a non-precious catalyst for the oxygen reduction reaction. J. Mater. Chem. A Mater. *3*, 3343–3350.
45. Wang, C., Li, Z., Wang, L., Niu, X., and Wang, S. (2019). Facile Synthesis of 3D Fe/N Codoped Mesoporous Graphene as Efficient Bifunctional Oxygen Electrocatalysts for Rechargeable Zn–Air Batteries. ACS Sustain. Chem. Eng. *7*, 13873–13885.
46. Li, Y.W., Zhang, W.J., Li, J., Ma, H.Y., Du, H.M., Li, D.C., Wang, S.N., Zhao, J.S., Dou, J.M., and Xu, L. (2020). Fe-MOF-Derived Efficient ORR/OER Bifunctional Electrocatalyst for Rechargeable Zinc-Air Batteries. ACS Appl. Mater. Interfaces *12*, 44710–44719.
47. Kone, I., Xie, A., Tang, Y., Chen, Y., Liu, J., Chen, Y., Sun, Y., Yang, X., and Wan, P. (2017). Hierarchical Porous Carbon Doped with Iron/Nitrogen/Sulfur for Efficient Oxygen Reduction Reaction. ACS Appl. Mater. Interfaces *9*, 20963–20973.
48. Niu, Y., Huang, X., and Hu, W. (2016). Fe3C nanoparticle decorated Fe/N doped graphene for efficient oxygen reduction reaction electrocatalysis. J. Power Sources *332*, 305–311.
49. Pan, T., Liu, H., Ren, G., Li, Y., Lu, X., and Zhu, Y. (2016). Metal-free porous nitrogen-doped carbon nanotubes for enhanced oxygen reduction and evolution reactions. Sci. Bull. *61*, 889–896.
50. Liu, J., Xu, L., Deng, Y., Zhu, X., Deng, J., Lian, J., Wu, J., Qian, J., Xu, H., Yuan, S., et al. (2019). Metallic cobalt nanoparticles embedded in sulfur and nitrogen co-doped rambutan-like nanocarbons for the oxygen reduction reaction under both acidic and alkaline conditions. J. Mater. Chem. A Mater. *7*, 14291–14301.
51. Wu, Z.Y., Xu, X.X., Hu, B.C., Liang, H.W., Lin, Y., Chen, L.F., and Yu, S.H. (2015). Iron Carbide Nanoparticles Encapsulated in Mesoporous Fe-N-Doped Carbon Nanofibers for Efficient Electrocatalysis. Angew. Chem., Int. Ed. Engl. *54*, 8179–8183.
52. Lin, L., Zhu, Q., and Xu, A.W. (2014). Noble-metal-free Fe–N/C catalyst for highly efficient oxygen reduction reaction under both alkaline and acidic conditions. J. Am. Chem. Soc. *136*, 11027–11033.
53. Perazzolo, V., Brandiele, R., Durante, C., Zerbetto, M., Causin, V., Rizzi, G.A., Cerri, I., Granozzi, G., and Gennaro, A. (2018). Density Functional Theory (DFT) and Experimental Evidences of Metal–Support Interaction in Platinum Nanoparticles Supported on Nitrogen- and Sulfur-Doped Mesoporous Carbons: Synthesis, Activity, and Stability. ACS Catal. *8*, 1122–1137.
54. Qiu, Y., Huo, J., Jia, F., Shanks, B.H., and Li, W. (2016). N- and S-doped mesoporous carbon as metal-free cathode catalysts for direct biorenewable alcohol fuel cells. J. Mater. Chem. A Mater. *4*, 83–95.
55. Zhang, X., Truong-Phuoc, L., Liao, X., Tuci, G., Fonda, E., Papaefthymiou, V., Zafeiratos, S., Giambastiani, G., Pronkin, S., and Pham-Huu, C. (2021). An Open Gate for High-Density Metal Ions in N-Doped Carbon Networks: Powering Fe–N–C Catalyst Efficiency in the Oxygen Reduction Reaction. ACS Catal. *11*, 8915–8928.
56. Han, J., Meng, X., Lu, L., Bian, J., Li, Z., and Sun, C. (2019). Single-Atom Fe-N x -C as an Efficient Electrocatalyst for Zinc–Air Batteries. Adv. Funct. Mater. *29*.
57. Ma, L., Li, J., Zhang, Z., Yang, H., Mu, X., Gu, X., Jin, H., Chen, D., Yan, S., Liu, S., and Mu, S. (2021). Atomically dispersed dual Fe centers on nitrogen-doped bamboo-like carbon nanotubes for efficient oxygen reduction. Nano Res. *15*, 1966–1972.
58. Li, B., Sasikala, S.P., Kim, D.H., Bak, J., Kim, I.-D., Cho, E., and Kim, S.O. (2019). Fe-N4 complex embedded free-standing carbon fabric catalysts for higher performance ORR both in alkaline & acidic media. Nano Energy *56*, 524–530.
59. Huang, H., Yu, D., Hu, F., Huang, S.C., Song, J., Chen, H.Y., Li, L.L., and Peng, S. (2022). Clusters Induced Electron Redistribution to Tune Oxygen Reduction Activity of Transition Metal Single-Atom for Metal-Air Batteries. Angew. Chem., Int. Ed. Engl. *61*, e202116068.
60. Zhang, N., Zhou, T., Ge, J., Lin, Y., Du, Z., Zhong, C., Wang, W., Jiao, Q., Yuan, R., Tian, Y., et al. (2020). High-Density Planar-like Fe2N6 Structure Catalyzes Efficient Oxygen Reduction. Matter *3*, 509–521.
61. Wu, X., Dong, J., Qiu, M., Li, Y., Zhang, Y., Zhang, H., and Zhang, J. (2020). Subnanometer iron clusters confined in a porous carbon matrix for highly efficient zinc–air batteries. Nanoscale Horiz. *5*, 359–365.
62. Liu, D., Wu, C., Chen, S., Ding, S., Xie, Y., Wang, C., Wang, T., Haleem, Y.A., ur Rehman, Z., Sang, Y., et al. (2018). In situ trapped high-density single metal atoms within graphene: Iron-containing hybrids as

representatives for efficient oxygen reduction. Nano Res. *11*, 2217–2228.
63. Chen, Y., Ji, S., Wang, Y., Dong, J., Chen, W., Li, Z., Shen, R., Zheng, L., Zhuang, Z., Wang, D., and Li, Y. (2017). Isolated Single Iron Atoms Anchored on N-Doped Porous Carbon as an Efficient Electrocatalyst for the Oxygen Reduction Reaction. Angew. Chem., Int. Ed. Engl. *56*, 6937–6941.
64. Ao, X., Zhang, W., Li, Z., Li, J.G., Soule, L., Huang, X., Chiang, W.H., Chen, H.M., Wang, C., Liu, M., and Zeng, X.C. (2019). Markedly Enhanced Oxygen Reduction Activity of Single-Atom Fe Catalysts via Integration with Fe Nanoclusters. ACS Nano *13*, 11853–11862.
65. Liu, M., Lee, J., Yang, T.C., Zheng, F., Zhao, J., Yang, C.M., and Lee, L.Y.S. (2021). Synergies of Fe Single Atoms and Clusters on N-Doped Carbon Electrocatalyst for pH-Universal Oxygen Reduction. Small Methods *5*, e2001165.
66. Sun, X., Song, P., Zhang, Y., Liu, C., Xu, W., and Xing, W. (2013). A class of high performance metal-free oxygen reduction electrocatalysts based on cheap carbon blacks. Sci. Rep. *3*, 2505.
67. Sun, Y., Zhang, W., Wang, Q., Han, N., Núñez-Delgado, A., Cao, Y., Si, W., Wang, F., and Liu, S. (2021). Biomass-derived N,S co-doped 3D multichannel carbon supported Au@Pd@Pt catalysts for oxygen reduction. Environ. Res. *202*, 111684.
68. Xiao, Z., Wu, Y., Cao, S., Yan, W., Chen, B., Xing, T., Li, Z., Lu, X., Chen, Y., Wang, K., and Jiang, J. (2021). An active site pre-anchoring and post-exposure strategy in Fe(CN)64-@PPy derived Fe/S/N-doped carbon electrocatalyst for high performance oxygen reduction reaction and zinc-air batteries. Chem. Eng. J. *413*, 127395.
69. Zhang, B., Wang, C., Liu, D., Liu, Y., Yu, X., and Wang, L. (2018). Boosting ORR Electrocatalytic Performance of Metal-Free Mesoporous Biomass Carbon by Synergism of Huge Specific Surface Area and Ultrahigh Pyridinic Nitrogen Doping. ACS Sustain. Chem. Eng. *6*, 13807–13812.
70. Liang, Y., Li, Y., Wang, H., Zhou, J., Wang, J., Regier, T., and Dai, H. (2011). Co(3)O(4) nanocrystals on graphene as a synergistic catalyst for oxygen reduction reaction. Nat. Mater. *10*, 780–786.
71. Huang, Z., Pan, H., Yang, W., Zhou, H., Gao, N., Fu, C., Li, S., Li, H., and Kuang, Y. (2018). In Situ Self-Template Synthesis of Fe-N-Doped Double-Shelled Hollow Carbon Microspheres for Oxygen Reduction Reaction. ACS Nano *12*, 208–216.
72. Borghei, M., Lehtonen, J., Liu, L., and Rojas, O.J. (2018). Advanced Biomass-Derived Electrocatalysts for the Oxygen Reduction Reaction. Adv. Mater. *30*, e1703691.
73. Wang, M., Yang, W., Li, X., Xu, Y., Zheng, L., Su, C., and Liu, B. (2021). Atomically Dispersed Fe–Heteroatom (N, S) Bridge Sites Anchored on Carbon Nanosheets for Promoting Oxygen Reduction Reaction. ACS Energy Lett. *6*, 379–386.
74. Zhu, X., Zhang, D., Chen, C.-J., Zhang, Q., Liu, R.-S., Xia, Z., Dai, L., Amal, R., and Lu, X. (2020). Harnessing the interplay of Fe–Ni atom pairs embedded in nitrogen-doped carbon for bifunctional oxygen electrocatalysis. Nano Energy *71*, 104597.
75. Jiang, L., Duan, J., Zhu, J., Chen, S., and Antonietti, M. (2020). Iron-Cluster-Directed Synthesis of 2D/2D Fe-N-C/MXene Superlattice-like Heterostructure with Enhanced Oxygen Reduction Electrocatalysis. ACS Nano *14*, 2436–2444.
76. Tran, T.-N., Song, M.Y., Singh, K.P., Yang, D.-S., and Yu, J.-S. (2016). Iron–polypyrrole electrocatalyst with remarkable activity and stability for ORR in both alkaline and acidic conditions: a comprehensive assessment of catalyst preparation sequence. J. Mater. Chem. A Mater. *4*, 8645–8657.
77. Li, Q., Chen, W., Xiao, H., Gong, Y., Li, Z., Zheng, L., Zheng, X., Yan, W., Cheong, W.C., Shen, R., et al. (2018). Fe Isolated Single Atoms on S, N Codoped Carbon by Copolymer Pyrolysis Strategy for Highly Efficient Oxygen Reduction Reaction. Adv. Mater. *30*, e1800588.
78. Lu, C., Zhang, J., Chen, Z., Jiang, K., Li, M., Zhang, F., Tong, G., Zou, X., Su, Y., and Zhuang, X. (2019). A room-temperature interfacial approach towards iron/nitrogen co-doped fibrous porous carbons as electrocatalysts for the oxygen reduction reaction and Zn-Air batteries. Nanoscale *11*, 10257–10265.
79. Yang, J., Wang, X., Li, B., Ma, L., Shi, L., Xiong, Y., and Xu, H. (2017). Novel Iron/Cobalt-Containing Polypyrrole Hydrogel-Derived Trifunctional Electrocatalyst for Self-Powered Overall Water Splitting. Adv. Funct. Mater. *27*.
80. Zheng, H., Zhang, Y., Long, J., Li, R., and Gou, X. (2020). Nitrogen-Doped Porous Carbon Material Derived from Biomass of Beancurd as an Efficient Electrocatalyst for Oxygen Reduction and Zn-air Fuel Cell. J. Electrochem. Soc. *167*, 84516.

STAR★METHODS

KEY RESOURCES TABLE

REAGENT or RESOURCE	SOURCE	IDENTIFIER
Chemicals, peptides, and recombinant proteins		
Cobalt chloride hexahydrate	Analytical Pure	Shanghai Maclean's Biochemical Technology Co.
Potassium carbonate anhydrous	Analytical Pure	Sinopharm Chemical Reagent Co.
Potassium hydroxide	Superior Purity	Shanghai Maclean's Biochemical Technology Co.
Ammonium persulfate	Analytical Pure	Shanghai Maclean's Biochemical Technology Co.
Ferric chloride hexahydrate	Analytical Pure	Shanghai McLean Biochemical Technology Co.
Isopropyl alcohol	Analytical Pure	Sinopharm Chemical Reagent Co.
Pt/C	20wt %	Johnson Matthey (JM)
Nafion	5wt %	DuPont
Methanol	Analytically pure	Sinopharm Chemical Reagent Co.
Oxygen	High Purity	Zibo Zhangdian Runshi Hardware Co.
Nitrogen	High Purity	Zibo Zhangdian Runshi Hardware Co.
Glucono-delta-lactone	/Analytical Pure	Shanghai New Lolo Foods Co.
Soya	/	Aurant Shopping Plaza
Other		
Scanning Electron Microscope (SEM)	Sirion 200	Frequency Electronics, Inc
Transmission Electron Microscope (TEM)	Tecnai G2F 20	Frequency Electronics, Inc
X-ray Diffractometer (XRD)	D8 Advance	Bruker, Inc
X-ray Photoelectron Spectroscopy (XPS)	ESCALAB 250Xi	Thermo Scientific, Inc
Raman Spectrometer (Raman)	HR Evolution Horiba	HORIBA Scientific, Inc
Specific surface area and porosity analyser (BET)	IQ3	Kantar Corporation. , Inc
Freeze Dryer	SJIA-10N-50A	Ningbo Shuangjia Instrument Co.
Tube Furnace	OTF-1200X	Hefei Kejing Material Technology Co.
Collector-type constant temperature magnetic stirrer	DF-101S	Gongyi Yuhua Instrument Co.
Ultrasonic cleaner	1730T	Beijing Kexi Century Technology Co.

RESOURCE AVAILABILITY

Lead contact

Further information and requests for resources and reagents should be directed to and will be fulfilled by the lead contact, Dr. Ning Han (ninghan51@126.com or ning.han@kuleuven.be).

Materials availability

This study did not generate new unique materials.

Data and code availability

The authors declare that the data supporting the findings of this study are available within the article and the supplemental information. Other data and results supporting the present study are available from the lead contact upon request.

METHOD DETAILS

Material synthesis and characterization

Reagents and apparatus

Soybean were bought from the local market and fresh tofu was made in the laboratory. Glucono-Delta-Lactone was purchased from ShangHai Xinluoluo Co., Ltd. Hydrochloric acid (HCl), anhydrous potassium carbonate (K_2CO_3) and isopropanol were purchased from Sinopharm Chemical Reagent Co., Ltd. Methanol, ferric chloride hexahydrate ($FeCl_3 \cdot 6H_2O$), zinc acetate ($Zn(CH_3COO)_2$) and potassium hydroxide

(KOH) were obtained from Macklin Biochemical Co., Ltd. The commercial Pt/C catalyst (20 wt %) and Nafion (5 wt %) were obtained from Johnson Matthey and Dupont, respectively. Ultrapure water (18.25 MΩ cm^{-1}) was from the laboratory. All chemicals were analytically pure.

Characterizations

Transmission electron microscopy (TEM) images, scanning transmission electron microscopy (STEM) images, and energy dispersive spectroscopy (EDS) line profiles were obtained using a FEI Tecnai G2T20. X-ray photoelectron spectroscopy (XPS) analysis was carried out using a K-Alpha ESCA system (Thermo Scientific). Scanning electron microscopy (SEM) was used to study the morphology of the modified electrode on an FEI SIRION microscope. Raman spectra were used to analyze graphitic ordering by a LabRAM HR800 from JY Horiba. CHI660E electrochemical system (CH Instrument, Shanghai, China) was used for all the electrochemical measurement. A conventional three-electrode system was used for all electrochemical experiments. Platinum wire (1 cm^2) and Ag/AgCl were selected as the counter electrode and reference electrode, respectively. A bare or modified glassy carbon electrode (GCE) (5 mm diameter) was used as working electrode.

Electrocatalytic measurements

The catalyst ink was prepared by dispersing 4.0 mg of catalyst in 1010 μL of solution containing 200 μL of isopropanol, 800 μL of water and 10 μL of 5 wt. % Nafion solution followed by ultrasonication for 30 min. A 10 μL portion of the resulting catalyst ink was loaded onto the end of a 5 mm diameter glassy carbon electrode. The electrolyte used was 0.1 M KOH solution. All of the electrochemical tests were performed on a PINE electrochemical instrument. Cyclic voltammograms of the electrocatalysts were obtained with a scan rate of 50 mV s^{-1} in O_2-saturated 0.1 M KOH. ORR polarization curves were recorded in O_2-saturated 0.1 M KOH at a rotating speed of 625, 900, 1225,1600 and 2025 rpm with a scan rate of 10 mV s^{-1}. The chronoamperometric measurement (i-t) was tested to evaluate the electrode stability at 0.5 V vs. RHE in O2-saturated 0.1 M KOH.

The Koutecky–Levich equation was used to calculate the kinetic current, which can be described as follows:

$$\frac{1}{j} = \frac{1}{j_k} + \frac{1}{j_d} = \frac{1}{j_k} + \frac{1}{B\omega^{1/2}}$$

Where j is the measured current density, j_k and j_d are the kinetic and diffusion-limited current densities, respectively. ω is the electrode rotating rate, and B could be determined from the slope of the K-L plots based on the Levich equation as follows:

$$B = 0.62nF(Do)^{2/3}\vartheta^{-1/6}Co$$

Where n represents the electron transfer number, F is the Faraday constant, D_o is the diffusion coefficient of O_2 in 0.1 M KOH, ϑ is the kinetic viscosity and C_o is the bulk concentration of O_2.

A home-built Zn-air battery was fabricated to further evaluate the electrocatalytic performance of the prepared Fe-NSC-800 catalyst. The Zn-air battery is composed of a polished Zn foil as the anode, catalyst loaded carbon cloths (catalyst loading amount of 1 mg cm^{-2}) as the air cathode, and 6.0 M KOH containing 0.2 M Zn(OAc)2·2H2O solution as the electrolyte. The galvanostatic charge-discharge cycling (5 min charge and 5 min discharge at a current density of 10 mA cm^{-2}) was performed in a NEWARE (CT-1008-5V6A-S1-F, neware) testing system. The electronic load instrument(M9700, Maynuo Company, Nanjing, China) was used to evaluated the galvanostatic discharge curves and Power density of Zn-air battery.

Calculation method

The DFT calculations are performed by the PW module contained in the Quantum ESPRESSO distribution. The nuclei and core electrons interactions were described by the projector augmented wave (PAW) method under generalized gradient approximation (GGA) using the Perdew-Burke-Ernzerhof (PBE) function. The kinetic energy cutoff of 30 Ry with the charge-density cutoff of 300 Ry were employed to ensure the convergence for the energy. The Fermi-surface effects has been treated by the smearing technique of Methfessel and Paxton, using a smearing parameter of 0.02 Ry. The k-point mesh of 3 × 3×1 was used for k-point sampling in the Brillouin-zones. The vacuum layer was ~15 Å to remove the slab interaction between the z direction. The models of three kinds of gN-Fe, prN-Fe and pdN-Fe had been relaxed before calculated to optimize the structure. The computational hydrogen electrode (CHE) model suggested by Nørskov et al. was introduced in the calculation of the Gibbs free energy change (ΔG) in all of step. We divided ORR reaction into four steps:

$$O2 + H+ + e- + * \rightarrow OOH*$$

$$OOH* + H+ + e- \rightarrow O* + H_2O$$

$$O* + H+ + e- \rightarrow OH*$$

$$OH* + H+ + e- \rightarrow * + H_2O$$

in which * implies the adsorption site. Subsequently, ΔG of the ORR steps were calculated by the following equation:

$$\Delta G = \Delta EDFT + \Delta ZPE - TS$$

where ΔEDFT is the electronic energy obtained from DFT calculations, zero-point energy (ZPE), and the entropy (S) of each adsorbed state, T is the temperature (T = 300 K).